Full length article

Influence of grain boundaries on the radiation-induced defects and hydrogen in nanostructured and coarse-grained tungsten

G. Valles [a, *], M. Panizo-Laiz [a], C. González [a, b], I. Martin-Bragado [c], R. González-Arrabal [a], N. Gordillo [a], R. Iglesias [d], C.L. Guerrero [a], J.M. Perlado [a], A. Rivera [a]

[a] Instituto de Fusión Nuclear UPM, José Gutiérrez Abascal, 2, 28006, Madrid, Spain
[b] Departamento de electrónica y Tecnología de Computadores, Universidad de Granada, Fuente Nueva & CITIC, Aynadamar, E-18071, Granada, Spain
[c] IMDEA Materials Institute, C/ Eric Kandel, 2, 28906, Getafe, Madrid, Spain
[d] Departamento de Física, Universidad de Oviedo, C/ Calvo Sotelo, s/n, Oviedo, Spain

ABSTRACT

We have studied the influence of grain boundaries (GBs) on the radiation-induced defect evolution and on H retention at 300 K, both experimentally and by computer simulations. For this purpose, coarse-grained tungsten (CGW) and nanostructured tungsten (NW) samples were implanted with H and C ions at energies of 170 keV and 665 keV respectively. Three different sets of experiments were carried out: (i) H single implantation, (ii) C and H co-implantation and (iii) C and H sequential implantation. Computer simulations were performed by using the Object Kinetic Monte Carlo (OKMC) methodology, which was parameterized by new and pre-existing Density Functional Theory (DFT) data. The three sets of experiments were simulated in monocrystalline tungsten (MW) and NW, resulting that (i) GBs have a clear influence on the amount and distribution of vacancies, being the vacancy concentration larger in NW than in MW samples, (ii) H retention is highly influenced by both the GBs themselves and the vacancy concentration, (iii) the size of H_nV_m clusters is slightly influenced by the presence of GBs and (iv) it can be inferred, from the comparison between experimental and computational results, that GBs act as preferential paths for H diffusion.

© 2016 Acta Materialia Inc. Published by Elsevier Ltd. All rights reserved.

1. Introduction

Due to its outstanding properties, tungsten is considered one of the most promising candidates as plasma-facing material (PFM) in future fusion reactors, both in magnetic (MC) and in inertial confinement (IC) approaches [1—5]. In principle, W is supposed to fulfill the majority of the highly demanding requirements, such as transient temperatures and stresses which will take place in a laser fusion chamber [6,7]. However, light species such as hydrogen [8,9] and helium [10,11] tend to nucleate in defects resulting in detrimental effects such as cracking, exfoliation or blistering, which is unacceptable for a PFM. Therefore, there is a need to develop materials capable to withstand the expected harsh conditions (extreme irradiation and large thermal loads) taking place in this kind of reactors.

In the case of direct drive targets in IC, H ions are expected to reach the PFM at high enough energies to produce Frenkel pairs (FPs), i.e., vacancies (Vs) and self-interstitial atoms (SIAs) [3]. According to the literature, H diffusivity in W strongly depends on the presence of vacancies, since H atoms get easily trapped at them with a high binding energy [12—16]. Nanostructured materials have a large density of GBs which, depending on the irradiation conditions, have a large influence on the distribution of both FPs and light species such as H. FPs have been described to annihilate at GBs under certain conditions [17—19]. However, the H behaviour at GBs is still unclear. On the one hand, some authors showed that H atoms experience enhanced diffusion along GBs with a migration energy lower than in the bulk [20,21]. Thus, GBs might act as preferential diffusion paths for H atoms [22]. On the other hand, other works report that the migration energy along the GB is higher than in the bulk [23]. Therefore, the physical mechanism for H behaviour at

* Corresponding author.
E-mail address: gonzalovallesalberdi@hotmail.com (G. Valles).

GBs is not well understood. Another important point about H trapping at GBs is whether H gets trapped at vacancies formed in the GBs or in their vicinity, or at GBs themselves. The fact that the formation energy of vacancies in the GB region [20,21] is lower than that in the bulk [24] may facilitate the trapping of H atoms at vacancies formed at the GBs. Thus, the role of vacancies in the case of the observed H concentration enhancement at the GB region is not clear [23,25].

In this study, we investigate the H behaviour in three varieties of tungsten with different GB densities: nanostructured tungsten (NW) with a large GB density, coarse-grained tungsten (CGW) with a lower GB density and monocrystalline tungsten (MW), with no GBs at all. The goal is to contribute to a better understanding of the role of GBs on the H behaviour in W at a temperature of 300 K. For this purpose, we compare experimental measurements to theoretical results calculated with the MMonCa [26,27] code, an Object Kinetic Monte Carlo (OKMC) simulator. The code is parameterized by a Density Functional Theory (DFT) database, which provides the required input for the OKMC simulations applied to NW and MW subject to different irradiation scenarios: (i) H single implantation (NW-H and MW-H), (ii) C and H co-implantation (NW-Co-CH and MW-Co-CH) and (iii) sequential C and H implantation (NW-Seq-CH and MW-Seq-CH), see Table 1. The simulation conditions were selected to mimic the experiments. The H and V distribution as well as the type and size of H_nV_m clusters are analyzed in detail in order to assess the influence of the GB density on them. The simulation results show that the density of radiation-induced vacancies is larger in NW than in MW samples. The reason stems from the fact that FPs exhibit a much higher recombination rate in MW than in NW samples. The resulting higher vacancy concentration in NW compared to MW leads to a higher H retention. Finally, by comparing the experimental and computational data, we conclude that GBs act as efficient migration paths for H.

2. Experiments

Pure α-phase, nanocrystalline W coatings preferentially oriented along the α-(110) direction, with a thickness of ~1.2 μm and a root mean square (rms) roughness lower than 3 nm were deposited by DC magnetron sputtering from a pure (99.95%) W commercial target at a normal incidence angle on a single-side polished Si (100) substrate. The deposition setup consists of a high vacuum chamber with a base pressure in the 10^{-6} Pa range, equipped with a 5 cm diameter magnetron designed and manufactured by Nano4Energy SL [28]. Deposition took place in the presence of a pure argon atmosphere (99.9999%) at room temperature. The Ar pressure was 8×10^{-1} Pa, the plasma power was 45 W and the target—substrate distance was 8 cm. The coatings are constituted of columns that grow perpendicular to the substrate, presenting an inverted pyramidal shape (compatible with the zone T in the Thornton's morphology diagram [29]) having a diameter of ~100 nm at the coating surface. A more detailed description of the morphological and microstructural properties of the coatings is found in Ref. [30].

In order to study the influence of the sample microstructure on H behaviour, two types of W samples were selected: the first type is the previously mentioned home-made nanostructured W and the second type is commercial CGW with a grain size in the μm range, supplied by Goodfellow. A first set of samples was implanted with H (NW-H and CGW-H cases). In order to study the influence of the irradiation induced damage and of the microstructure on the H behaviour a second set of samples was sequentially implanted first with C and then with H (NW-Seq-CH and CGW-Seq-CH cases). In order to assess the influence of the synergistic effects on the radiation-induced damage and on H retention, a third set of samples was simultaneously implanted with C and H (NW-Co-CH and CGW-Co-CH cases). All implantations were performed at room temperature. In order to mimic IC energies in future HiPER-type power plants, the implantation energies were selected to be 170 keV and 665 keV for H and C, respectively [31]. The implantation fluence for both H and C was 5×10^{16} cm^{-2}. Irradiation conditions are summarized in Table 1. The implantations were performed at the Helmholtz-Zentrum Dresden-Rossendorf (HZDR). Prior to implantation and in order to achieve a higher depth resolution when carrying out Resonant Nuclear Reaction Analysis (RNRA) experiments, the CGW samples were mechanically polished by using napless synthetic cloth. For the first rough polishing step a 0.5 μm colloidal alumina was used. The second polishing was done by using a 0.03 μm colloidal alumina. The CGW samples were not heated either before or after polishing. The NW samples did not undergo any treatment (neither polishing nor heating) before implantation because their rms was lower than 3 nm.

The H depth profiles were characterized by RNRA experiments, using the H(^{15}N,αγ)^{12}C nuclear reaction [32] with a N^{2+} beam impinging onto the sample surface at normal incidence. This reaction has a sharp resonance at 6.385 MeV. The beam energy was varied in the range from 6.425 to 11.033 MeV. The 4.43 MeV γ-rays were detected by a 10×10 cm^2 BGO detector mounted immediately outside the vacuum chamber at about 1.5 cm behind the sample. Some special precautions were taken in order to carry out reliable depth profiling measurements and to avoid ion beam-induced hydrogen diffusion [33]. The beam spot and the current were selected to be 2×2 mm^2 and ~10 nA, respectively. In addition, the beam spot position was changed every two measurements. As described in Ref. [34], in order to ensure that the selected experimental configuration does not lead to ion beam-induced diffusion, several spectra were sequentially measured on the same point up to a dose 10 times higher than that used in these experiments. No ion beam-induced hydrogen diffusion was detected in any case. More

Table 1
Experimental and simulated irradiation conditions for MW (simulations), CGW (experiments) and NW (simulations and experiments).

Sample code	Type of W	Type of study	H irradiation		C irradiation		Comment
			Energy (keV)	Fluence (cm^{-2})	Energy (keV)	Fluence (cm^{-2})	
MW-H	Monocrystalline	Computational	170	5×10^{16}	–	–	–
CGW-H	Coarse-grained	Experimental	170	5×10^{16}	–	–	–
NW-H	Nanocrystalline	Computational and experimental	170	5×10^{16}	–	–	–
MW-Co-CH	Monocrystalline	Computational	170	5×10^{16}	665	5×10^{16}	C and H simultaneous implantation
CGW-Co-CH	Coarse-grained	Experimental	170	5×10^{16}	665	5×10^{16}	C and H simultaneous implantation
NW-Co-CH	Nanocrystalline	Computational and experimental	170	5×10^{16}	665	5×10^{16}	C and H simultaneous implantation
MW-Seq-CH	Monocrystalline	Computational	170	5×10^{16}	665	5×10^{16}	H implanted after C implantation
CGW-Seq-CH	Coarse-grained	Experimental	170	5×10^{16}	665	5×10^{16}	H implanted after C implantation
NW-Seq-CH	Nanocrystalline	Computational and experimental	170	5×10^{16}	665	5×10^{16}	H implanted after C implantation

details about RNRA characterization are given in Ref. [35].

3. Simulation methods

3.1. Density Functional Theory (DFT) calculations

Binding energies for H_nV_m clusters were obtained by performing calculations based on DFT techniques, using the *Vienna Ab initio Simulation Package* (VASP) [36–38]. The PBE [39] parameterization of the Generalized Gradient Approximation (GGA) for the exchange and correlation functional was used, as well as the Plane Augmented Wave pseudopotentials [40] provided by the code. In the case of W, six valence electrons were considered (4 $3d$ and 2 $4s$) and 1 $1s$ in the case of H. The lattice parameter was estimated to be 3.172 Å (using an energy cutoff for the plane waves of 479 eV), which is in good agreement with the experimental result of 3.165 Å [41]. We built the $5 \times 5 \times 5$ cubic supercell (250 W atoms) by repeating the unit cell five times along each direction while 8 k-points (a $2 \times 2 \times 2$ mesh) sampled the first Brillouin zone. Up to 10 H atoms were placed in the unit cell in the case of a single vacancy (V) whereas up to 4 H atoms were placed in the case of V_2, V_3 and V_4. All the structures were fully relaxed until the forces on all atoms were smaller than 0.025 eV/Å. From the total energy, the formation and binding energies were obtained. These data were subsequently used in the OKMC simulations.

Formation energies (E_f) for a system of a certain number of W and H atoms, N_W and N_H, respectively, were calculated as follows [16]:

$$E_f = E_{tot} - N_W E(W) - N_H E(H), \tag{1}$$

where E_{tot} is the final total energy, $E(W)$ is the atomic energy of one tungsten atom inside the pure bulk when a $5 \times 5 \times 5$ supercell is used and $E(H)$ is half the energy of the isolated H_2 molecule [16,42,43], located inside an otherwise empty $5 \times 5 \times 5$ supercell with sides equal to the equilibrium lattice parameter of the pure W. The binding energy, E_b, corresponds to the energy released when two (or more) objects merge to become a single one. The general expression for E_b for a system with a number of defects N_{def} defects (including vacancies, SIAs or H atoms) can be written as [16]:

$$E_b\left(N_{def}\right) = \sum_{i_{def}=1}^{N_{def}} E_f\left(i_{def}\right) - E_f\left(N_{def}\right). \tag{2}$$

In Eq. (2), the binding energy is defined as the difference between a system in which the objects are close together and a system in which the objects are far apart. For that reason, the formation energy of the configurations where the objects are separated is usually calculated in an individual supercell for each object, as defined in Eq. (1).

3.2. Object Kinetic Monte Carlo (OKMC) simulations

OKMC simulations were performed with the Open Source code MMonCa [26,27,44]. The code was parameterized to simulate H irradiation in tungsten making use of our own DFT calculations for H atoms trapped in vacancies [16,21]. Binding energies for H_nV_m clusters are summarized in Table 2. In the case of H trapped in a single vacancy (for H configurations, see Ref. [16]), our results are in good agreement with previously published data [12–15]. Up to 10 H atoms trapped in a single vacancy were calculated. Although in Refs. [13,15] only up to 6 H atoms were calculated, Johnson et al. [15] suggested that more than 6 H atoms could be trapped in a monovacancy, as stated in Ref. [43]. In addition, binding energies

Table 2
Binding energy of a H atom to a mixed H_nV_m cluster or to a pure V_m cluster calculated by DFT simulations.

Cluster	Binding energy (eV)
HV (H → V)	1.20
H_2V (H → HV)	1.19
H_3V (H → H_2V)	1.07
H_4V (H → H_3V)	0.95
H_5V (H → H_4V)	0.87
H_6V (H → H_5V)	0.52
H_7V (H → H_6V)	0.5
H_8V (H → H_7V)	0.46
H_9V (H → H_8V)	0.17
$H_{10}V$ (H → H_9V)	0.20
HV_2 (H → V_2)	0.97
H_2V_2 (H → HV_2)	0.28
H_3V_2 (H → H_2V_2)	2.60
H_4V_2 (H → H_3V_2)	0.85
HV_3 (H → V_3)	2.01
H_2V_3 (H → HV_3)	1.29
H_3V_3 (H → H_2V_3)	1.00
H_4V_3 (H → H_3V_3)	0.82
HV_4 (H → V_4)	1.87
H_2V_4 (H → HV_4)	1.71
H_3V_4 (H → H_2V_4)	1.11
H_4V_4 (H → H_3V_4)	0.51

for H atoms to V_2, V_3 and V_4 clusters were calculated (see Table 2). Binding energies (as a function of the H/V ratio) for larger clusters were calculated by approximating the DFT data to the following power law:

$$E_b(H \rightarrow H_{n-1}V_m) = 1.04 \cdot \left(\frac{n}{m}\right)^{-0.43}, \tag{3}$$

where E_b is the binding energy and n/m is the H/V ratio of the resulting cluster. However, these approximated values have a slight influence on the results. Since the migration energy of vacancies is 1.66 eV [24], the great majority of H atoms are retained in mono-vacancies (see Section 4). In the case of pure V_m and I_m clusters, the values were taken from Ref. [24]. Pure hydrogen clusters (H_n) cannot be formed in bulk W due to the large repulsive energy between H atoms, as has extensively been reported [45,46]. SIAs bind to H atoms with $E_b = 0.33$ eV [24]. Due to this low binding energy, SIAs do not trap H atoms at 300 K, similarly to the results of Ref. [47].

Concerning migration parameters, values for single vacancy (V), pure vacancy clusters (V_m), single SIA (I) and pure SIA clusters (I_m) were taken from Becquart et al. [24]. In the case of the migration energy of a single H atom, our DFT calculations gave a value of 0.205 eV, which is in perfect agreement with previously published data [12,48]. Mixed H_nV_m and H_nI_m clusters were considered immobile. It has been reported that the H_1V_1 cluster can migrate ($E_m = 2.52$ eV [12]), but this high energy barrier effectively suppresses the migration of H_1V_1 clusters at the temperature considered in this work (300 K). Migration energies of single defects are summarized in Table 3.

Table 3
Migration energy (eV) of single H atoms, SIAs and single vacancies in tungsten.

Defect	Migration energy (eV)
H	0.205
I (SIA)	0.013 [24]
V	1.66 [24]

A simulation box of $10 \times 10 \times 1000$ (depth) nm^3 was used for the MW system. Periodic boundary conditions (PBCs) were imposed in the four lateral surfaces. Thus, GBs were completely ignored. Attempts were done to simulate CGW. However, the computational cost of simulating grains of the order of micros was too high. The influence of GBs on H retention was analyzed by comparing the simulation results (for MW and NW) and the experimental results (for CGW and NW). In the case of nano-structured tungsten (NW), a simulation box of $50 \times 50 \times 1000$ (depth) nm^3 was used. In order to reproduce the GBs, the four lateral surfaces were considered as perfect sinks, i.e., all the defects (vacancies, SIAs and H atoms) that reached GBs were removed out of the simulation. We only take into account the H atoms present in the interior of the grain, not those that reach the GBs. In both MW and NW, the top surface was considered as a desorption surface, whereas atoms reaching the bottom surface were considered to move further deep into the bulk and thus ignored.

A concern regarding the chosen small simulation boxes is related to the lateral straggling of the incoming H and C ions (236 and 220 nm, respectively), which is much larger than the lateral dimensions of the simulation boxes. We checked whether the small boxes have an influence on the final H and V concentration profiles. For this purpose, simulations with boxes of larger dimensions (surface area up to 200×200 nm^2) were carried out for a lower irradiation time. The results (not shown) reveal little effect on the H and V concentration profiles in all cases, regardless of the box dimensions. Thus, the chosen small boxes are appropriate for the irradiation conditions used in this paper.

Damage cascades produced by C and H implantation were calculated with the SRIM code [49,50]. It is worthwhile to mention that SRIM calculates the final position of both vacancies and incident ions (H or C) but not the position of SIAs. Therefore, the position of SIAs was calculated by following the methodology described in Ref. [51], where a thermalization distance that follows a Gaussian distribution with the range and straggling values obtained by SRIM is assumed. Although SRIM does not take into account the temperature effect (i.e., the formation of clusters of defects), the subsequent OKMC simulation takes into account this effect. However, neither C nor H irradiation in W (300 K) produce vacancy clusters, as vacancies do not migrate due to their high migration energy (1.66 eV), except in special cases in which vacancies upon thermalization end up so close to each other that they can react. Moreover, in the case of small vacancy clusters formed during the C irradiation, these small vacancy clusters would be formed at depths between 350 and 450 nm, far from the main H retention peak (at depth between 600 and 800 nm) in NW (see Section 4) and thus, their influence on H retention would be negligible.

In order to mimic the irradiation conditions taking place during the experiments, the damage cascades (FPs and H ions) produced by H irradiation were introduced in the simulation box at a flux of 2.78×10^{12} cm^{-2} s^{-1} during 5 h, reaching a fluence of 5×10^{16} cm^{-2}, at a temperature of 300 K. The same irradiation conditions were considered in the case of C irradiation. In order to get a more detailed simulation of the experimental conditions, after the implantation a subsequent annealing (300 K during 10 days) was simulated. Thus, the period of time between the experimental irradiation and the analysis of the samples was also taken into account. The results show the H retention and V concentration after this annealing. For simplicity, in the case of C irradiation the FPs produced by the irradiation were introduced in the simulation box, but not the C ions. This approximation is justified by the fact that C atoms do not trap H atoms in W. Ou et al. [52] have recently described that C, in interstitial position, is not capable of capturing H atoms efficiently because of Coulomb repulsion between negatively charged C and H atoms in W. In the case that C atoms are in substitutional positions, i.e., bound to a vacancy, they are able to trap H atoms, as stated in Refs. [52,53]. However, substitutional C can only appear in significant number if either C atoms or vacancies can migrate. Due to the large migration energy of C ($E^m = 1.69$ eV [54]) and V($E^m = 1.66$ eV [24]), both can be considered immobile at 300 K. Ahlgren et al. [47] published that impurities play a significant role as they decrease Frenkel pair annihilation by trapping SIAs. However, SIA trapping at 300 K is not important, since the binding energy of C atoms to SIAs is lower than 0.5 eV [13,24]. Moreover, impurities have not been considered in the simulations because the vacancy concentration ($\sim 10^{20}$–10^{21} cm^{-3}) is much higher than the expected impurity concentration ($\sim 10^{18}$ cm^{-3} [53], 30 ppm in our CGW samples). For this reason, the H retention at impurities is expected to play a minor role.

4. Results

As shown in Fig. 1(a), the implantation ranges of vacancies generated by H (170 keV) and C (665 keV) in tungsten are around 550 and 400 nm respectively, as obtained by SRIM simulations. C ions are responsible for the great majority of vacancies. The calculated number of FPs produced per incoming ion is on average 363 for C and 2.3 for H. As evidenced in Fig. 1(b), GBs dramatically affect the vacancy concentration. The vacancy profiles calculated
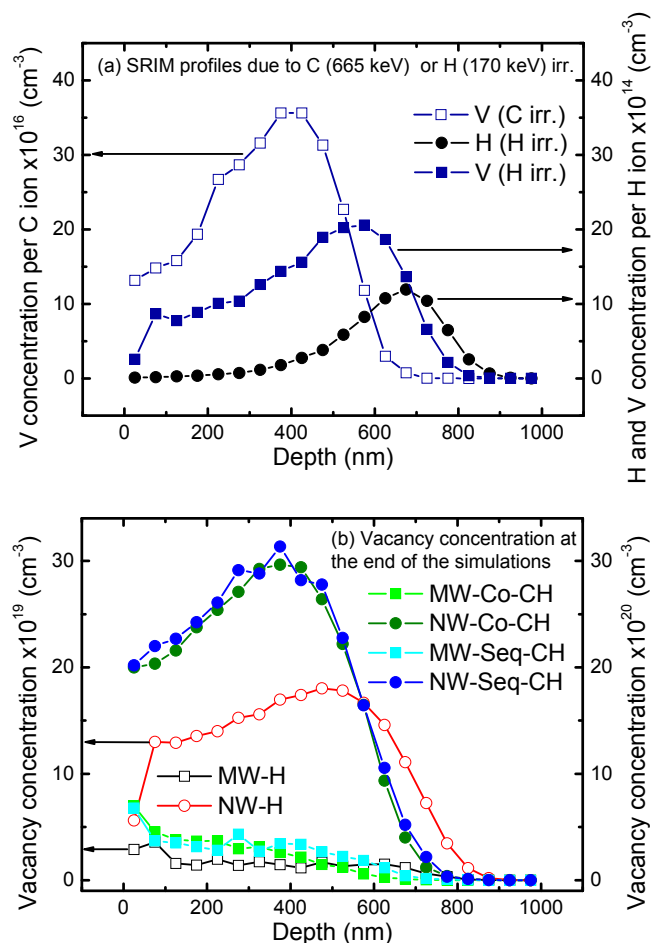

Fig. 1. (a) Vacancy concentration as a function of depth per C or H ion as calculated by the SRIM code. Also H concentration is also shown. (b) Vacancy concentration as a function of the depth at the end of the simulations, after the process of annihilation between Vs and SIAs as calculated by the MMonCa code.

with OKMC show that the vacancy concentration is systematically much higher in NW (high GB density) than in MW (no GBs). In MW, most of the vacancies annihilate with SIAs, whereas in NW a much higher fraction (around 9 times higher) of vacancies survives after the irradiation due to the efficient role of GBs as sinks for (highly mobile) SIAs, as shown in Table 4.

Regarding H concentration, the attention is focused on the region between 150 and 1000 nm, where the radiation-induced damage is mainly generated. We refer to it as the "damaged region". It is important to stand out that the experimentally observed high H retention at the surface region (Fig. 2) was not simulated. Although a surface effect on H desorption from the surface has been reported [55], the high near surface H concentration observed in our experiments is mainly related to surface contamination [35]. In this study, all the simulation results refer to H and defects present in the interior of the grain, and not at the GBs. Hydrogen is trapped in H_nV_m clusters (in fact, mainly in monovacancies). There is no H trapped in SIAs, as the binding energy between SIAs and H atoms is very low. Due to their low migration energy, SIAs and pure SIA clusters either annihilate with vacancies or reach the free surfaces, leading to a total absence of SIAs at the end of the simulations. Interestingly, the H profile calculated with MMonCa resembles the H profile predicted by SRIM for all the NW implantation cases, but not for the GB-free material (MW), as shown in Fig. 1(a). Thus, H atoms are trapped near their implantation positions, obtaining a very good agreement between simulations and experiments in all NW cases. This indicates efficient H trapping at vacancies in NW samples, whereas in MW samples, the shape of H profiles indicates clear H diffusion.

In the case of MW-H irradiation, since only 2.3 vacancies per H ion are generated, there is a very high diffusion of H atoms, leading to only 7.6% retention after the irradiation and the subsequent 10 days annealing, see Fig. 2(a). Since there are no GBs at all, the annihilation between vacancies and SIAs leads to a low vacancy concentration and thus, few trapping sites for H atoms. As a result, the simulated H profile (MW-H) is almost constant in the "damaged volume", since H atoms diffuse all along the depth direction. In the case of experimental results in CGW-H, a higher H retention between 300 and 800 nm appears, as shown in Fig. 2(a). In this case, the GBs present in the sample lead to a lower annihilation rate among vacancies and SIAs, as some of the SIAs will reach the GBs before finding a vacancy to annihilate with. Thus, there should be a higher vacancy concentration and a higher H retention. On the contrary, in the case of NW-H (both simulations and experiments),

there is a higher H retention, see Fig. 2(b). As GB density increases, the annihilation between vacancies and SIAs decreases, leading to a higher vacancy concentration in the interior of the grain. H atoms are retained between 600 and 800 nm in depth, which corresponds to the H implantation range calculated with the SRIM code, see Fig. 1. H atoms are trapped near their implantation positions, implying that there is low H diffusion.

Carbon and hydrogen simultaneous irradiation leads to different results, which can be observed in Fig. 2(c) and (d). In the NW-Co-CH case, the simulated H profile is in good agreement with the experimental one. In addition, the total H retention is almost the same in the simulations (46.5%) as in the experiments (42.0%). Comparing the MW-Co-CH case (simulations) with the CGW-Co-CH (experiments), it can be observed that there is a higher H retention between 150 and 540 nm and a lower H retention between 540 and 1000 nm in MW-Co-CW, see Fig. 2(c) and Table 4. In MW-Co-CH, the main H retention peak appears at ~400 nm. This result stems from the absence of GBs in MW-Co-CH. Since H atoms cannot reach any GB, their only way to diffuse is along the irradiation direction (X direction). In their migration to the irradiation surface, H atoms reach a region highly populated by vacancies at ~400 nm, which leads to a high trapping rate of H atoms in those vacancies. This explains the differences in the H profile between 150 and 540 nm. A possible explanation for the experimentally measured H retention at depths >800 nm would be that H is trapped in other defects apart from vacancies, for instance dislocations [56] to which H atoms can migrate thanks to the low vacancy population as compared to the experimental NW-Co-CH.

In the NW-Seq-CH case, see Fig. 2(f), the simulated H profile is in good agreement with the experimental one, as in the previous case, showing a H retention peak at ~650 nm in depth in both experiments and simulations. In addition, the total retained fraction observed experimentally corresponds with that obtained from the simulations (42.0% and 53.2%, respectively). In the case of MW-Seq-CH (simulations), a much higher H retention is observed when comparing to CGW-Seq-CH (experiments), see Table 4. Again, there is a much higher H retention in the case of MW-Seq-CH, as the simulations ignore the GBs, and H atoms can only diffuse along the X direction. When H atoms reach the region highly populated by vacancies at ~400 nm, they are trapped inside these vacancies.

Concerning the type and size of clusters at which H atoms are trapped, all the simulations show the same trend: more than 90% of H atoms are retained in monovacancies with different H content (Fig. 3). The migration energy for a single vacancy is so high that

Table 4
Total H retained fraction between 150 and 1000 nm, at 300 K, measured from experiments or calculated with MMonCa just after the irradiation or after the subsequent annealing during 10 days at 300 K. Also the remaining vacancies (%) are shown.

Sample code	Exp. H retention (%)	MMonCa H retention (%) just after C and/or H irradiation	MMonCa H retention (%) after 10 days annealing	MMonCa remaining vacancies (%) after 10 days annealing
MW-H	–	11.6	7.6	0.9
CGW-H	17.0	–	–	–
NW-H	31.0	33.0	32.4	9.3
MW-Co-CH	–	57.4 (150–540 nm)	58.1 (150–540 nm)	0.1
CGW-Co-CH	25.0 (150–540 nm)	–	–	–
NW-Co-CH	42.0	46.5	46.2	0.8
MW-Seq-CH	–	94.7	94.3	0.1
CGW-Seq-CH	42.0	–	–	–
NW-Seq-CH	48.0	53.2	53.0	0.9

282

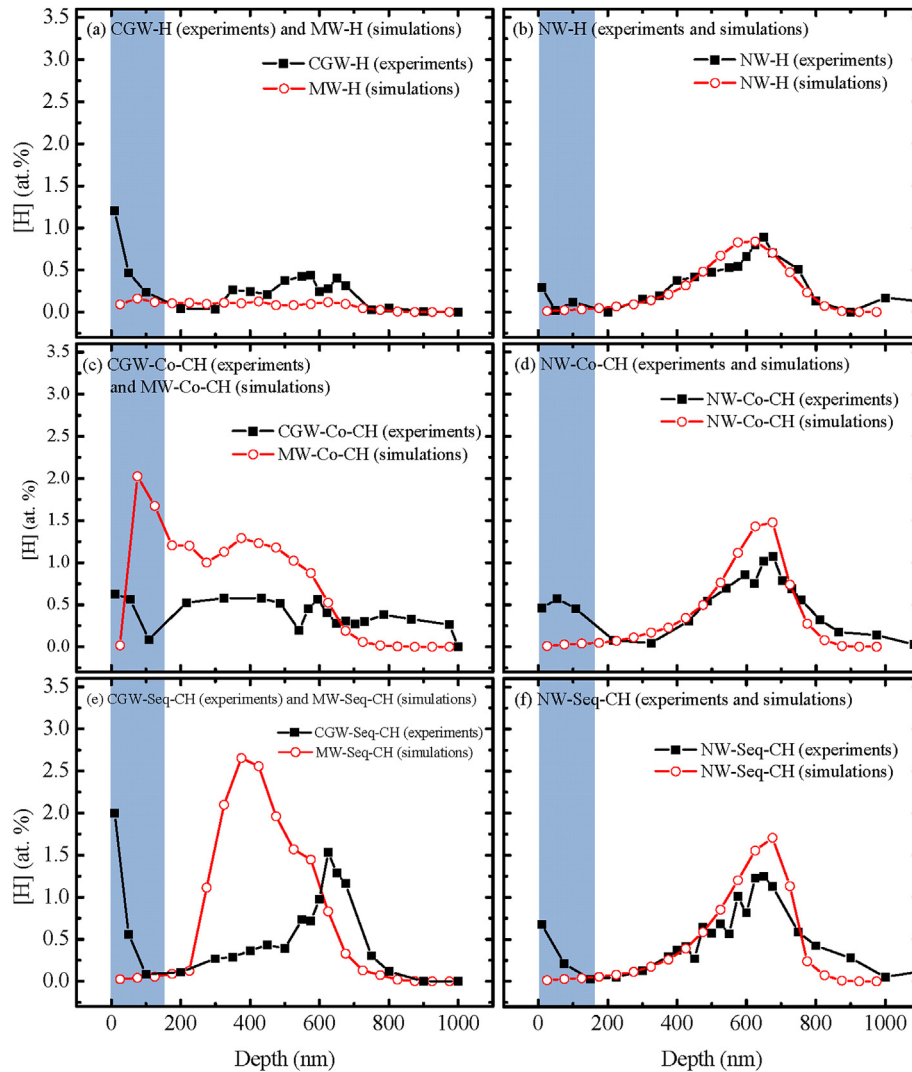G. Valles et al. / Acta Materialia 122 (2017) 277–286

Fig. 2. H concentration as a function of depth in CGW (experiments) or MW (simulations), and NW (both experiments and simulations), depending on the irradiation conditions: H single implantation for CGW or MW (a) and for NW (b), C and H co-implanted for CGW or MW (c) and NW (d) and C and H sequential implantation for CGW or MW (e) and NW (f). The simulation results are calculated after the annealing of 10 days at 300 K. The region between 0 and 150 nm (in blue) has been taken into account neither in the results nor in the discussion because it is highly influenced by surface contamination [35].

vacancies turn out to be immobile at 300 K. Thus, the formation of vacancy clusters is prevented either in MW or in NW, regardless of the type of irradiation.

5. Discussion

Our OKMC parameterization for H irradiation in W reproduces a variety of irradiation conditions on different samples at 300 K. Furthermore, the experimentally observed discrepancies in the case of low grain boundary density (CGW) and high grain boundary density (NW) results can be explained with the aid of the simulations.

Hydrogen atoms get trapped at vacancies forming mixed H_nV_m clusters. As described in Section 3.2, H atoms cannot form pure H clusters (H_n). Thus, the process of "self-trapping" described for He in W [57], i.e., the emission of a W atom from its lattice position creating a vacancy in which He atoms get trapped, is not possible in this case. In addition, the H-SIA trapping mechanism at 300 K is inefficient due to its low binding energy (0.33 eV). Therefore, the retention of H is determined by the density and distribution of

surviving vacancies (those that did not annihilate with SIAs). The initial cascades provided by SRIM shown in Fig. 1(a) correspond to the FP profile assuming no annihilation. If annihilation is considered, the vacancy profiles clearly differ from the SRIM ones, as shown in Fig. 1(b). At 300 K vacancies are immobile, unlike highly mobile SIAs (Table 3) which are able to annihilate with vacancies, at free surfaces or at grain boundaries (at lateral surfaces in our simulations). In all the cases concerning NW, the maximum H retention in both experiments and simulations is observed between 600 and 700 nm (Fig. 2), which corresponds to the H range as calculated by SRIM. This means that H atoms easily get trapped at vacancies near their as-implanted position, due to the large concentration of vacancies (recall that the simulated H profiles shown in Fig. 2 do not include H atoms that reached GBs). On the other hand, in MW simulations higher vacancy annihilation rate occurs (around 9 times higher than in NW in all the simulations). The resulting vacancy profile completely differs with respect to that predicted by SRIM, resulting in an almost constant vacancy concentration all along the "damaged region". This can be observed comparing Fig. 1(a)–(b). Due to this low vacancy concentration for
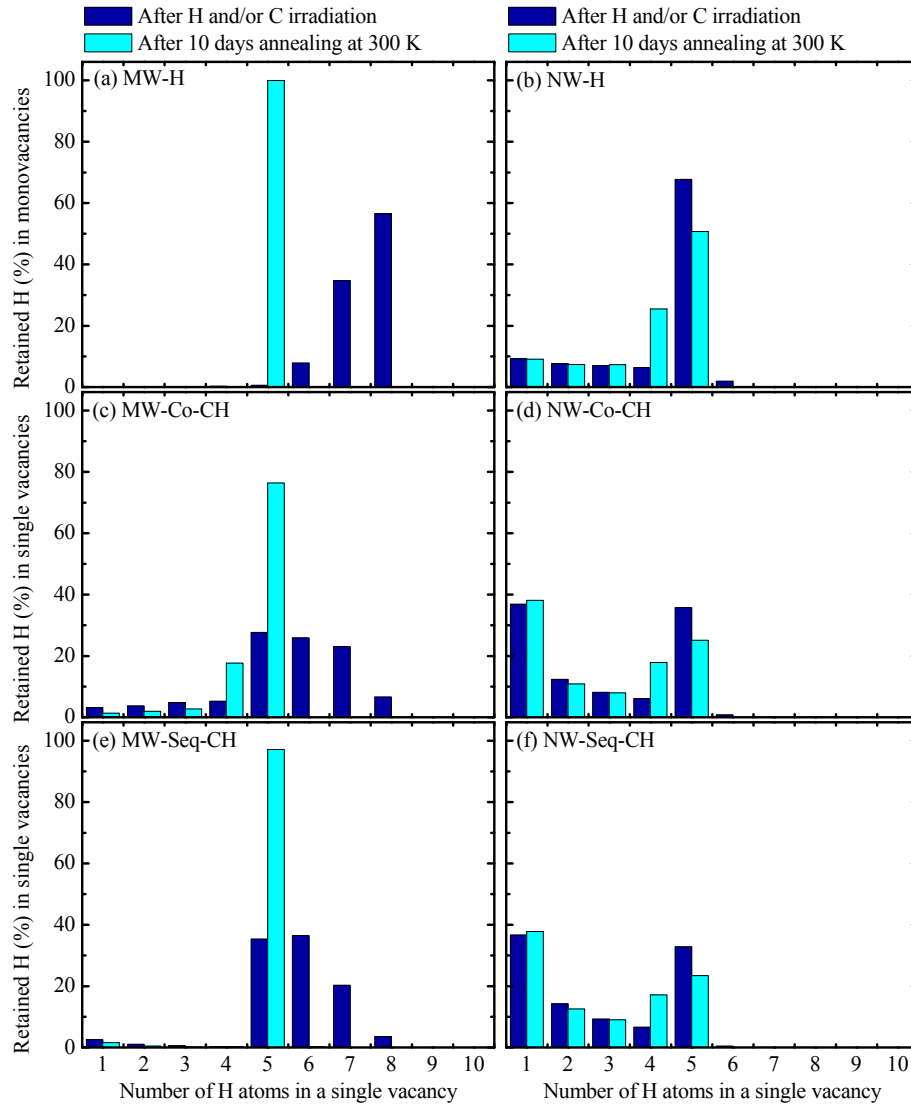
Fig. 3. Retained H fraction with respect of the total H retained in monovacancies, as a function of the H atoms in the monovacancy, from H_1V_1 to $H_{10}V_1$, in all the cases simulated: single H irradiation in MW (a) and NW (b), C and H simultaneously irradiated in MW (c) and NW (d), and C and H sequentially irradiated in MW (e) and NW (f) in both just after the ion irradiation and after the subsequent annealing during 10 days at 300 K.

MW samples, the H atoms are able to migrate along bulk W and get trapped at vacancies far away from their initial positions. Since GBs are completely ignored in MW simulations, the lower vacancy concentration leads to the discrepancies observed between the computational (MW) and the experimental (CGW) results.

As previously mentioned, nanostructured materials (high GB density) are considered as "self-healing" materials under certain circumstances [17] due to the enhanced annihilation of FPs at GBs, as reported for Cu [58,59], Cu-Nb interfaces [60] and W [61]. Indeed, the effect is rather general in metals [18,19]. The interaction of vacancies and SIAs at GBs can be explained by a three-step process, depending on the temperature of the metal, as described in Refs. [19,62]. Firstly, due to their high mobility, SIAs migrate and get trapped at GBs. At low temperatures, the process ends at this stage, resulting in a higher vacancy density in nanostructured materials as compared to monocrystalline ones [63,64]. Secondly, at intermediate temperatures, the SIAs retained at the GBs are emitted, migrate inside grains and annihilate more vacancies. Thirdly, at high temperatures, vacancies become mobile and migrate, finding GBs at which they annihilate. The whole "self-healing" process can explain the experimental results in nanostructured and polycrystalline Au reported by Chimi et al. in Ref. [65]. These authors reported that the defect accumulation rate in nanocrystalline Au at ~15 K is larger than in polycrystalline Au (here only the first step takes place). On the contrary, at 300 K, defect accumulation becomes much smaller than in polycrystalline Au (where the three steps are taken into account), showing the "self-healing" behaviour of nanocrystalline metals. In our case, the simulations were carried out also at 300 K. However, at this temperature only the first step is expected to take place in W, contrary to what happens in Au. This is because both formation (E_f $(V)_W \approx 3.23$ eV, $E_f (V)_{Au} \approx 0.94$ eV) and migration (E_m $(V)_W \approx 1.66$ eV, $E_m (V)_{Au} \approx 0.71$ eV) energies are much higher for W than for Au [24,66—68]. Therefore, the needed temperature for each of the previously described steps to take place is higher for W than for Au. Our simple model, which considers GBs as perfect sinks, turns out good enough to reproduce the first step, responsible for the higher vacancy density in NW than in MW.

On the other hand, H behaviour at GBs can be deduced from the comparison between our experimental and computational results
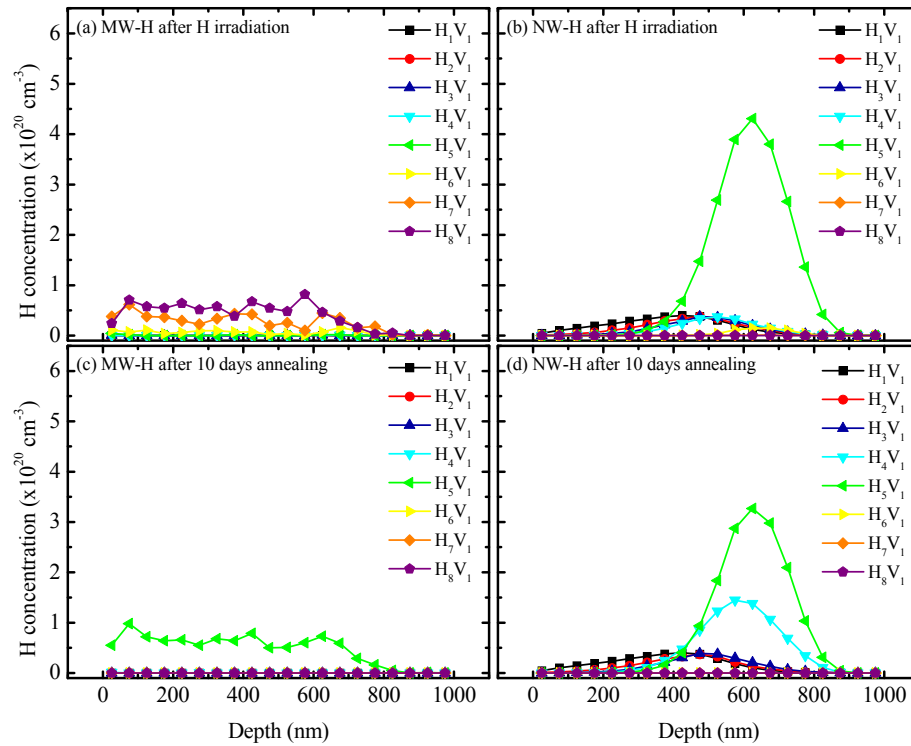
Fig. 4. H concentration as a function of depth arranged by cluster type (H_nV_1). In the case of single H irradiation in both MW-H just after H irradiation (a) and after an annealing of 10 days at 300 K (c) and NW-H, also in the case just after H irradiation (b) and after an annealing of 10 days at 300 K (d).

in the case of NW. Our simulated H profiles only include H atoms in the interior of the grain. Since simulations and experiments agree regarding both the total H fraction and the H profile, a major conclusion is that H atoms that reach the GBs can migrate along them towards the surface and desorb. This is in good agreement with data reported by Zhou et al. [20] about the influence of symmetric GBs on H atoms in W. Their DFT calculations gave a H migration barrier of 0.13 eV along the GBs, i.e., 0.07 eV lower than the value (0.2 eV) in the bulk. The diffusion barrier for H becomes lower when it approaches the GB, suggesting that H atoms cannot easily escape out of the GB [20]. We have published similar results [21] in a non-coherent interface formed by two W(110) and W(112) surfaces. Thus, DFT results in different interfaces and, in addition, MD studies [22] support the idea that H atoms get trapped at GB regions, diffusing along them. Nevertheless, other works carried out at higher temperatures (T > 300 K) show that H is retained at GBs. Yu et al. [25] observed H retention at GBs at temperatures ranging from 600 K to 1200 K whilst Piaggi et al. [23] obtained similar results between 1200 and 2000 K. However, at such high temperatures more physical processes might take place apart from those described at 300 K in the present paper, for instance, vacancy formation in the vicinity of GBs. The value of the formation energy of a vacancy from a GB in W has been published in Refs. [20,21]. This value ($E_f(V)_{GB} = 1.6$ eV) is much lower than the formation energy of a vacancy in bulk tungsten ($E_f(V)_{Bulk} = 3.23$ eV) [24]. This means that at temperatures higher than 300 K (around 650 K), vacancies might be formed at grain boundaries, being able to efficiently trap H atoms. We pointed out in a recent publication that the GBs might act as trapping sites for H atoms [35]. In our theoretical DFT analysis [21], we showed that the H atoms prefer the vacancy at the GB. Nevertheless, the experimental results showed a clear trend, namely, the higher the GB density the higher the retained H fraction. However, the comparison between experimental and OKMC results clarifies that, although this is so, the trend is not related to H

trapping at GBs but to the effect that GBs have on FP annihilation at 300 K, resulting in a higher vacancy concentration and consequently, a higher H retention.

With regard to C irradiation, the experimental and OKMC results show a lower influence on H retention in the case of NW (Fig. 2). In addition, Table 4 shows that C irradiation results in a less pronounced H retention enhancement in NW than in MW. This also supports the idea of the GBs acting as diffusion paths for H atoms. The presence of a higher GB density in NW leads to a higher probability of H release along GBs, being less affected by the presence of the higher vacancy concentrations induced by C irradiation. On the contrary, in MW cases, H atoms must cross the high vacancy density region in their way to the surface, which leads to a larger H retention in these samples than in NW. Moreover, comparing MW-Co-CH and MW-Seq-CH, a clear influence of the irradiation procedure itself, either simultaneous or sequential C and H implantation, is observed, even though the concentration of vacancies is similar in both cases, see Fig. 1(b). In MW-Seq-CH case, the previous C irradiation creates a huge number of vacancies leading to a higher H retention, as H atoms must cross the "damaged region" to reach the desorption surface.

An interesting outcome of the simulations is the determination of the type and size of H_nV_m clusters. Simulations reveal that the presence of some H_nV_m clusters with more than one vacancy ($m > 1$) only occurs when a vacancy is created in the vicinity of a pre-existing one, as vacancies do not migrate at 300 K. This implies that in all the simulations independently of the density of GBs or irradiation conditions, more than 90% of H atoms are retained in H_nV_1 clusters, i.e., in monovacancies. Fig. 3 shows the results of H trapped in monovacancies (%), as a function of the number of H in the monovacancy, just after H and/or C implantation and after the subsequent annealing of 10 days at 300 K. As described in Section 3, DFT calculations showed that up to 10 H atoms can be trapped in a single vacancy, with a binding energy that decreases as the H

content of the vacancy increases. All the NW simulations, regardless the type of C and/or H irradiation, show that no more than 5 H atoms are trapped by a monovacancy after ion irradiation. This corresponds to a binding energy for H_5V_1 ($H \rightarrow H_4V_1$) of 0.87 eV. The binding energies for the three next incorporated H atoms, i.e., H_6V_1, H_7V_1 and H_8V_1, are 0.52, 0.5 and 0.46 eV, respectively. Thus, at 300 K the temperature is high enough to enable slow H emission. On the other hand, the 5th H atom cannot be emitted at 300 K. In the case of MW, different results were obtained. On the one hand, just after the irradiation, H atoms are trapped at clusters such as H_5V_1, H_6V_1, H_7V_1 and H_8V_1. On the other hand, after the annealing of 10 days at 300 K, H atoms trapped in H_6V_1, H_7V_1 and H_8V_1 are emitted, leading to dominant formation of H_5V_1 clusters. This can be explained as follows. Just after the C and/or H irradiation, H atoms are trapped in H_6V_1, H_7V_1 and H_8V_1. However, they are unstable at 300 K and H atoms are constantly being emitted from these clusters and trapped in cluster nearby. After the 10 days annealing at 300 K, there is time enough to observe all the emissions of these clusters, the diffusion of the emitted H atoms and the subsequent trapping by other clusters or, in a very small number, the desorption at the irradiation surface. This effect is clearly shown in the case of MW-H and NW-H in Fig. 4.

Hodille et al. [69] reported that H atoms should be retained in three different types of traps, with binding energies of 0.83, 1.0 and 1.5 eV between 300 and 700 K. This is in good agreement with the our results, as the simulations reveal that the main trapping of H atoms is in monovacancies, from H_5V_1 to H_1V_1, with binding energies from 0.87 to 1.2 eV.

6. Conclusions

Experiments were performed to study H behaviour at 300 K in single H irradiation, simultaneous and sequential C and H implantation. In order to gain a better understanding of the experimental results, all the conditions were simulated with an OKMC code parameterized by DFT data. An overall good agreement between experimental and computational results was obtained in the case of NW. On the contrary, in the case of CGW, different results were obtained, as for computational reasons, monocrystalline W (MW) was simulated rather than CGW, i.e., no GBs at all were considered in this case.

The first conclusion is that the larger the GB density the higher the chance for fast SIAs to reach a GB before annihilating vacancies which, on the contrary, cannot move to reach any GB at room temperature. This leads to a higher vacancy density in NW than in CGW and, thus, a higher H retention in H_nV_m clusters formed in the interior of the grains. A second consequence of the vacancy immobility is that the great majority of H is retained in single vacancies (H_nV_1) in both MW and NW, having the GB density a small influence on the size of formed clusters. Moreover, if there is enough time for the unstable H_nV_1 clusters to emit all the H atoms at binding energies lower than 0.87 eV, all the H atoms are retained in clusters with a number of 5 H (H_5V_1) atoms or lower.

There is a very good agreement between experiments and simulations in the case of NW samples. Both the total H concentration and its distribution in depth measured in the experiments are well-reproduced by the theoretical results. For that reason, we conclude that in the experiments all the H atoms should be retained in the interior of the grains, and thus, that GBs may act as preferential paths for H atoms to diffuse in W at 300 K.

The comparison of the results presented in this paper with previous publications suggests a strong dependence of the irradiation temperature on the potential "self-healing" behaviour of nanostructured W. This really relevant result indicates that self-healing in W would happen at temperatures in which the

mobility of vacancies is activated. This fact together with the fact that GBs favour H release point out that nanostructured W may be a candidate for this kind of applications, as it exhibits a higher radiation resistance than the traditionally suggested CGW. However, there is still an open question when considering this kind of application which is related to the thermal stability of nanostructured W. This is a very important point not properly investigated so far.

Appendix A. Supplementary data

Supplementary data related to this article can be found at http://dx.doi.org/10.1016/j.actamat.2016.10.007.

References

[1] J.W. Davis, V.R. Barabash, A. Makhankov, L. Plöchl, K.T. Slattery, Assessment of tungsten for use in the ITER plasma facing components, Part 1, J. Nucl. Mater. 258—263 (1998) 308—312.

[2] M. Kaufmann, R. Neu, Tungsten as first wall material in fusion devices, Fusion Eng. Des. 82 (2007) 521—527.

[3] J. Alvarez Ruiz, A. Rivera de Mena, R. Gonzalez Arrabal, D. Garoz Gómez, E. del Rio Redondo, J.M. Perlado Martin, Materials research for HiPER laser fusion facilities: chamber wall, structural material and final optics, Fusion Sci. Technol. 60 (2011) 565—569.

[4] J.D. Sethian, A.R. Raffray, J. Latkowski, J.P. Blanchard, L. Snead, T.J. Renk, S. Sharafat, An overview of the development of the first wall and other principal components of a laser fusion power plant, J. Nucl. Mater. 347 (2005) 161—177.

[5] J.D. Sethian, D.G. Colombant, J.L. Giuliani, R.H. Lehmberg, M.C. Myers, S.P. Obenschain, A.J. Schmitt, J. Weaver, M.F. Wolford, F. Hegeler, M. Friedman, A.E. Robson, A. Bayramian, J. Caird, C. Ebbers, J. Latkowski, W. Hogan, W.R. Meier, L.J. Perkins, K. Schaffers, S. Abdel Kahlik, K. Schoonover, D. Sadowski, K. Boehm, L. Carlson, J. Pulsifer, F. Najmabadi, A.R. Raffray, M.S. Tillack, G. Kulcinski, J.P. Blanchard, T. Heltemes, A. Ibrahim, E. Marriott, G. Moses, R. Radell, M. Sawan, J. Santarius, G. Sviatoslavsky, S. Zenobia, N.M. Ghoniem, S. Sharafat, J. El-Awady, Q. Hu, C. Duty, K. Leonard, G. Romanoski, L.L. Snead, S.J. Zinkle, C. Gentile, W. Parsells, C. Prinksi, T. Kozub, T. Dodson, D.V. Rose, T. Renk, C. Olson, N. Alexander, A. Bozek, G. Flint, D.T. Goodin, J. Hund, R. Paguio, R.W. Petzoldt, D.G. Schroen, J. Sheliak, T. Bernat, D. Bittner, J. Karnes, N. Petta, J. Streit, D. Geller, J.K. Hoffer, M.W. McGeoch, S.C. Glidden, H. Sanders, D. Weidenheimer, D. Morton, I.D. Smith, M. Bobecia, D. Harding, T. Lehecka, S.B. Gilliam, S.M. Gidcumb, D. Forsythe, N.R. Parikh, S. O'Dell, M. Gorensek, The science and technologies for fusion energy with lasers and direct-drive targets, IEEE Trans. Plasma Sci. 38 (2010) 690—703.

[6] J.P. Blanchard, C.J. Martin, Thermomechanical effects in a laser IFE first wall, J. Nucl. Mater. 347 (2005) 192—206.

[7] A.R. Raffray, Threats, design limits and design windows for laser IFE dry wall chambers, J. Nucl. Mater. 347 (2005) 178—191.

[8] Y. Ueda, T. Funabiki, T. Shimada, K. Fukumoto, H. Kurishita, M. Nishikawa, Hydrogen blister formation and cracking behavior for various tungsten materials, J. Nucl. Mater. 337—339 (2005) 1010—1014.

[9] K. Tokunaga, M.J. Baldwin, R.P. Doerner, N. Noda, Y. Kubota, N. Yoshida, T. Sogabe, T. Kato, B. Schedler, Blister formation and deuterium retention on tungsten exposed to low energy and high flux deuterium plasma, J. Nucl. Mater. 337—339 (2005) 887—891.

[10] S.J. Zenobia, L.M. Garrison, G.L. Kulcinski, The response of polycrystalline tungsten to 30 keV helium ion implantation at normal incidence and high temperatures, J. Nucl. Mater. 425 (2012) 83—92.

[11] S.J. Zenobia, G.L. Kulcinski, Formation and retention of surface pores in helium-implanted nano-grain tungsten for fusion reactor first-wall materials and divertor plates, Phys. Scr. 2009 (2009) 14049.

[12] N. Fernandez, Y. Ferro, D. Kato, Hydrogen diffusion and vacancies formation in tungsten: density functional theory calculations and statistical models, Acta Mater. 94 (2015) 307—318.

[13] K. Heinola, T. Ahlgren, K. Nordlund, J. Keinonen, Hydrogen interaction with point defects in tungsten, Phys. Rev. B 82 (2010) 94102.

[14] K. Ohsawa, J. Goto, M. Yamakami, M. Yamaguchi, M. Yagi, Trapping of multiple hydrogen atoms in a tungsten monovacancy from first principles, Phys. Rev. B 82 (2010) 184117.

[15] D.F. Johnson, E.A. Carter, Hydrogen in tungsten: absorption, diffusion, vacancy trapping, and decohesion, J. Mater. Res. 25 (2010) 315—327.

[16] C. Guerrero, C. González, R. Iglesias, J.M. Perlado, R. González-Arrabal, First principles study of the behavior of hydrogen atoms in a W monovacancy, J. Mater. Sci. 51 (2015) 1445—1455.

[17] G. Ackland, Controlling radiation damage, Science 327 (2010) 1587—1588.

[18] X.-M. Bai, B.P. Uberuaga, The influence of grain boundaries on radiation-induced point defect production in materials: a review of atomistic studies, JOM 65 (2013) 360—373.

[19] I.J. Beyerlein, A. Caro, M.J. Demkowicz, N.A. Mara, A. Misra, B.P. Uberuaga, Radiation damage tolerant nanomaterials, Mater. Today 16 (2013) 443—449.

[20] H.-B. Zhou, Y.-L. Liu, S. Jin, Y. Zhang, G.-N. Luo, G.-H. Lu, Investigating behaviours of hydrogen in a tungsten grain boundary by first principles: from dissolution and diffusion to a trapping mechanism, Nucl. Fusion 50 (2010) 25016.

[21] C. González, M. Panizo-Laiz, N. Gordillo, C.L. Guerrero, E. Tejado, F. Munnik, P. Piaggi, E. Bringa, R. Iglesias, J.M. Perlado, R. González-Arrabal, H trapping and mobility in nanostructured tungsten grain boundaries: a combined experimental and theoretical approach, Nucl. Fusion 55 (2015) 113009.

[22] U. von Toussaint, S. Gori, A. Manhard, T. Höschen, C. Höschen, Molecular dynamics study of grain boundary diffusion of hydrogen in tungsten, Phys. Scr. 2011 (2011) 14036.

[23] P.M. Piaggi, E.M. Bringa, R.C. Pasianot, N. Gordillo, M. Panizo-Laiz, J. del Río, C. Gómez de Castro, R. Gonzalez-Arrabal, Hydrogen diffusion and trapping in nanocrystalline tungsten, J. Nucl. Mater. 458 (2015) 233—239.

[24] C.S. Becquart, C. Domain, U. Sarkar, A. DeBacker, M. Hou, Microstructural evolution of irradiated tungsten: ab initio parameterisation of an OKMC model, J. Nucl. Mater. 403 (2010) 75—88.

[25] Y. Yu, X. Shu, Y.-N. Liu, G.-H. Lu, Molecular dynamics simulation of hydrogen dissolution and diffusion in a tungsten grain boundary, J. Nucl. Mater. 455 (2014) 91—95.

[26] I. Martin-Bragado, A. Rivera, G. Valles, J.L. Gomez-Selles, M.J. Caturla, MMonCa: an Object Kinetic Monte Carlo simulator for damage irradiation evolution and defect diffusion, Comput. Phys. Commun. 184 (2013) 2703—2710.

[27] http://materials.imdea.org/MMonCa.

[28] http://www.nano4energy.eu.

[29] J.A. Thornton, Influence of substrate temperature and deposition rate on structure of thick sputtered Cu coatings, J. Vac. Sci. Technol. 12 (1975) 830—835.

[30] N. Gordillo, M. Panizo-Laiz, E. Tejado, I. Fernandez-Martinez, A. Rivera, J.Y. Pastor, C.G. de Castro, J. del Rio, J.M. Perlado, R. Gonzalez-Arrabal, Morphological and microstructural characterization of nanostructured pure α-phase W coatings on a wide thickness range, Appl. Surf. Sci. 316 (2014) 1—8.

[31] J. Alvarez, D. Garoz, R. Gonzalez-Arrabal, A. Rivera, M. Perlado, The role of spatial and temporal radiation deposition in inertial fusion chambers: the case of HiPER, Nucl. Fusion 51 (2011) 53019.

[32] J.R. Tesmer, M.A. Nastasi, Handbook of modern ion beam materials analysis, Mater. Res. Soc. (1995) 193—204.

[33] I.P. Chernov, Y.I. Tyurin, Y.P. Cherdantzev, M. Kröning, H. Baumbach, Hydrogen migration and release in metals and alloys at heating and radiation effects, Int. J. Hydrog. Energy 24 (1999) 359—362.

[34] R. Gonzalez-Arrabal, F. Munnik, M. González, P. Romero, R. Heller, F. Leardini, J.M. Perlado, Ion beam analysis of as-received, H-implanted and post implanted annealed fusion steels, Nucl. Instrum. Methods Phys. Res. Sect. B Beam Interact. Mater. A. T. 271 (2012) 27—32.

[35] R. Gonzalez-Arrabal, M. Panizo-Laiz, N. Gordillo, E. Tejado, F. Munnik, A. Rivera, J.M. Perlado, Hydrogen accumulation in nanostructured as compared to the coarse-grained tungsten, J. Nucl. Mater. 453 (2014) 287—295.

[36] G. Kresse, J. Furthmuller, Efficient iterative schemes for ab initio total-energy calculations using a plane-wave basis set, Phys. Rev. B 54 (1996) 11169—11186.

[37] G. Kresse, J. Hafner, Abinitio molecular-dynamics for liquid-metals, Phys. Rev. B 47 (1993) 558—561.

[38] G. Kresse, D. Joubert, From ultrasoft pseudopotentials to the projector augmented-wave method, Phys. Rev. B 59 (1999) 1758—1775.

[39] J.P. Perdew, K. Burke, M. Ernzerhof, Generalized gradient approximation made simple, Phys. Rev. Lett. 77 (1996) 3865—3868.

[40] P. Blochl, Projector augmented-wave method, Phys. Rev. B 50 (1994) 17953—17979.

[41] M.P. Lord, A.M. James, Biochem. Educ., Macmillan's Chemical and Physical Data, vol. 21, Macmillan, Basingstoke, 1993, pp. 109—110.

[42] C.S. Becquart, C. Domain, A density functional theory assessment of the clustering behaviour of He and H in tungsten, J. Nucl. Mater. 386—388 (2009) 109—111.

[43] Y.-L. Liu, H.-B. Zhou, Y. Zhang, Investigating behaviors of H in a W single crystal by first-principles: from solubility to interaction with vacancy, J. Alloys Compd. 509 (2011) 8277—8282.

[44] G. Valles, C. González, I. Martin-Bragado, R. Iglesias, J.M. Perlado, A. Rivera, The influence of high grain boundary density on helium retention in tungsten, J. Nucl. Mater. 457 (2015) 80—87.

[45] K.O.E. Henriksson, K. Nordlund, A. Krasheninnikov, J. Keinonen, Difference in formation of hydrogen and helium clusters in tungsten, Appl. Phys. Lett. 87 (2005) 163113.

[46] Y.-L. Liu, Y. Zhang, G.-N. Luo, G.-H. Lu, Structure, stability and diffusion of hydrogen in tungsten: a first-principles study, J. Nucl. Mater. 390—391 (2009) 1032—1034.

[47] T. Ahlgren, K. Heinola, K. Vörtler, J. Keinonen, Simulation of irradiation induced deuterium trapping in tungsten, J. Nucl. Mater. 427 (2012) 152—161.

[48] K. Heinola, T. Ahlgren, Diffusion of hydrogen in bcc tungsten studied with first principle calculations, J. Appl. Phys. 107 (2010) 13531.

[49] J.F. Ziegler, M.D. Ziegler, J.P. Biersack, SRIM — the stopping and range of ions in matter, Nucl. Instrum. Methods Phys. Res. Sect. B Beam Interact. Mater. A. T. 268 (2010) 1818—1823.

[50] http://www.srim.org/.

[51] G. Valles, A.L. Cazalilla, C. Gonzalez, I. Martin-Bragado, A. Prada, R. Iglesias, J.M. Perlado, A. Rivera, A multiscale approach to defect evolution in tungsten under helium irradiation, Nucl. Instrum. Methods Phys. Res. Sect. B Beam Interact. Mater. A. T. 352 (2015) 100—103.

[52] X.D. Ou, L.Q. Shi, K. Sato, Q. Xu, Y.X. Wang, Effect of carbon on hydrogen behaviour in tungsten: first-principle calculations, Nucl. Fusion 52 (2012) 123003.

[53] K. Heinola, T. Ahlgren, Hydrogen retention to impurities in tungsten: a multi-scale study, J. Nucl. Mater. 438 (2013) S1001—S1004.

[54] K. Nordlund, C. Björkas, T. Ahlgren, A. Lasa, A.E. Sand, Multiscale modelling of plasma—wall interactions in fusion reactor conditions, J. Phys. Appl. Phys. 47 (2014) 224018.

[55] J. Guterl, R.D. Smirnov, S.I. Krasheninnikov, B. Uberuaga, A.F. Voter, D. Perez, Modeling of hydrogen desorption from tungsten surface, J. Nucl. Mater 463 (2015) 263—267.

[56] D. Terentyev, V. Dubinko, A. Bakaev, Y. Zayachuk, W.V. Renterghem, P. Grigorev, Dislocations mediate hydrogen retention in tungsten, Nucl. Fusion 54 (2014) 42004.

[57] J. Boisse, C. Domain, C.S. Becquart, Modelling self trapping and trap mutation in tungsten using DFT and molecular dynamics with an empirical potential based on DFT, J. Nucl. Mater. 455 (2014) 10—15.

[58] X.-M. Bai, L.J. Vernon, R.G. Hoagland, A.F. Voter, M. Nastasi, B.P. Uberuaga, Role of atomic structure on grain boundary-defect interactions in Cu, Phys. Rev. B 85 (2012) 214103.

[59] W.Z. Han, M.J. Demkowicz, E.G. Fu, Y.Q. Wang, A. Misra, Effect of grain boundary character on sink efficiency, Acta Mater. 60 (2012) 6341—6351.

[60] X.-Y. Liu, B.P. Uberuaga, M.J. Demkowicz, T.C. Germann, A. Misra, M. Nastasi, Mechanism for recombination of radiation-induced point defects at inter-phase boundaries, Phys. Rev. B 85 (2012) 12103.

[61] C.G. Zhang, W.H. Zhou, Y.G. Li, Z. Zeng, X. Ju, Primary radiation damage near grain boundary in bcc tungsten by molecular dynamics simulations, J. Nucl. Mater. 458 (2015) 138—145.

[62] X.-M. Bai, A.F. Voter, R.G. Hoagland, M. Nastasi, B.P. Uberuaga, Efficient annealing of radiation damage near grain boundaries via interstitial emission, Science 327 (2010) 1631—1634.

[63] M. Samaras, P.M. Derlet, H.V. Swygenhoven, M. Victoria, Atomic scale modelling of the primary damage state of irradiated fcc and bcc nano-crystalline metals, J. Nucl. Mater. 351 (2006) 47—55.

[64] N.-Y. Park, P.-R. Cha, Y.-C. Kim, H.-K. Seok, S.-H. Han, S.-C. Lee, S. Cho, H. Jung, Radiation damage in nano-crystalline tungsten: a molecular dynamics simulation, Met. Mater. Int. 15 (2009) 447—452.

[65] Y. Chimi, A. Iwase, N. Ishikawa, M. Kobiyama, T. Inami, S. Okuda, Accumulation and recovery of defects in ion-irradiated nanocrystalline gold, J. Nucl. Mater. 297 (2001) 355—357.

[66] T. Kino, J.S. Koehler, Vacancies and divacancies in quenched gold, Phys. Rev. 162 (1967) 632—648.

[67] W. Triftshäuser, J.D. McGervey, Monovacancy formation energy in copper, silver, and gold by positron annihilation, Appl. Phys. 6 (1975) 177—180, http://dx.doi.org/10.1007/BF00883748.

[68] K. Sonnenberg, U. Dedek, Migration energy of single vacancies in gold, Radiat. Eff. 61 (1982) 175—178.

[69] E.A. Hodille, X. Bonnin, R. Bisson, T. Angot, C.S. Becquart, J.M. Layet, C. Grisolia, Macroscopic rate equation modeling of trapping/detrapping of hydrogen isotopes in tungsten materials, Part 1, J. Nucl. Mater. 467 (2015) 424—431.